International Journal of Remote Sensing, 2015
Vol. 36, No. 4, 979–999, http://dx.doi.org/10.1080/01431161.2014.1001087

Backprojection SAR interferometry

Michael I. Duersch* and David G. Long

Department of Electrical & Computer Engineering, Brigham Young University, Provo, UT 84602, USA

(*Received 9 September 2014; accepted 4 December 2014*)

Synthetic aperture radar (SAR) interferometry uses the phase difference between two SAR antennas to obtain an elevation estimate of the imaged terrain. Using an initial digital elevation model (DEM), the time-domain backprojection algorithm implicitly removes the terrain height phase from images during image formation. The use of a DEM during image formation adds additional information to the process of interferometry, resulting in different sensitivities to conventional interferometry. This article presents a novel method of SAR interferometry using backprojected imagery. It is shown that the sensitivity and performance of backprojection interferometry is significantly different to that of conventional methods. Specifically, it is shown that backprojection interferometry is much less sensitive to errors in measurement of the interferometric baseline length and angle. This comes at the expense of higher sensitivity to phase errors. We conclude that backprojection interferometry is best suited for airborne operation.

1. Introduction

In synthetic aperture radar (SAR), interferometry may be divided into two categories: along-track interferometry and cross-track interferometry (Melvin and Scheer 2013). Along-track interferometry uses multiple receive antennas separated in the along-track dimension in order to extract information about target motion in the imaged scene. Cross-track interferometry utilizes multiple receive antennas separated in the cross-track dimension (i.e. elevation and/or ground range) in order to determine the height of the imaged terrain (Franceschetti and Lanari 1999). Cross-track interferometry is employed in the generation of digital elevation models (DEMs) (Li and Goldstein 1990; Rodriguez and Martin 1992; Zebker and Villasenor 1992; Rosen et al. 2000; Zebker and Goldstein 1986). This article examines cross-track interferometry and from this point forward refers to it as simply interferometry.

Traditional SAR interferometry uses coherent images formed by frequency domain methods to produce a height map of the imaged surface. Because frequency domain methods are used, traditional interferometry is subject to two implicit assumptions: (1) the interferometric phase difference between the images is due to the propagation path length difference, and (2) imaging is in the slant plane. Because imaging is in the slant plane (which is different for each image), the two images must be co-registered. The time-domain backprojection algorithm (Duersch and Long 2015), however, produces images in the ground plane (ameliorating the need to co-register the two images) and the resulting pixels have a phase related to the difference between the expected propagation path length and the actual length. Thus, backprojected interferometric phase is a difference of differences (this

*Corresponding author. Email: mid@byu.net

point is clarified later). Because of this distinction in interferometric phase, a new, backprojection-oriented interferometric calculation is required to estimate terrain elevation.

Backprojection creates images in the ground plane and can use an initial estimate of the terrain elevation for image formation It is important to note that the use of a DEM during backprojection adds additional information to the interferometry problem. Thus, it is reasonable to anticipate a performance difference in interferometry performed with and without a DEM. (Note that the authors do not suggest that the performance difference between the methods is a result of clever processing.) The use of a reference DEM adds information to the process that alters sensitivities in a way that is particularly useful at low altitudes.

This article considers side-looking SAR interferometry for the time-domain backprojection algorithm. The article does not propose using backprojection interferometry in place of traditional interferometry, but rather seeks to explore the difference between each, and the strengths and weaknesses of both. Backprojection interferometry is derived, followed by an analysis of its characteristics and a comparison to traditional interferometry. It is seen that backprojection interferometry is much less sensitive than conventional interferometry to measurement errors in the interferometric baseline, and backprojection interferometry ameliorates phase unwrapping of the interferogram. Backprojection, however, is more sensitive to phase noise. We show that it is best suited for low-altitude use. Because SAR interferometry is used in a number of applications, this article does not limit itself to a single application, but rather attempts to provide analysis for general use.

The article is organized as follows. Section 2 derives backprojection interferometry for squint-less, side-looking SAR. Using these results, Section 3 compares the input parameter sensitivity of traditional interferometry to backprojection interferometry. Specific performance characteristics of backprojection interferometry are given in Section 4. Finally, Section 5 concludes with analysis of the results and recommendation of when backprojection interferometry is advantageous.

2. Backprojection interferometry derivation

The following derivation of time-domain backprojection interferometry assumes a side-looking, squint-less geometry with a narrow-beam antenna. As shown in Duersch and Long (2015), under these assumptions the phase of each backprojected pixel can be estimated as the residual phase at the point of closest approach. This makes a derivation of backprojection interferometry tractable.

The phase of a received coherent radar signal lends insight into the length of the propagation path that the signal travelled. Given a monostatic antenna A, the observed signal phase is a 2π wrapped equivalent of the distance times the carrier wavenumber ($k = 2\pi\ /\lambda$),

$$\phi = 2kr_a \bmod 2\pi, \tag{1}$$

where r_a is the one-way range from the antenna to a given target. Unfortunately, because of the phase wrapping, the range-resolution of the radar is typically not fine enough to unambiguously recover the exact distance the wave travelled. However, through the use of two receive antennas A and B, the *difference* in path length ($r_a - r_b$) between the two can be determined with great precision. Interferometry makes use of this fact in order to obtain the height of the imaged terrain.

The backprojection interferometric phase difference $\Delta\Phi$ of two collocated, backprojected pixels is

$$\Delta\Phi = 2k\left(\Delta r_a - \Delta r_b\right), \tag{2}$$

where k is the radar carrier wavenumber, and Δr is the backprojection residual range (Duersch and Long 2015), where the subscripts a and b refer to the *receive* antennas A and B, respectively. The quantity $(\Delta r_a - \Delta r_b)$ is the 'difference of differences' mentioned earlier. Note that any contribution due to the transmit antenna is explicitly neglected so long as the receive antennas share a common transmitter. We assume that there are no polarimetric phase effects, in which case the propagation phase from the transmitter to the scattering cell is common to both receive paths and is removed by the interferometric difference. The term *scattering cell* refers to the physical volume represented by a given pixel.

Backprojection removes the assumed phase component to the scattering cell, leaving a residual phase due to the unknown exact range to the phase centre of the scattering cell (Duersch and Long 2015). However, because the receive antennas are not collocated they do not observe precisely the same area. Figure 1(*a*) illustrates this in an exaggerated manner. Vectors **A** and **B** are the receive antenna locations, and **C** is the estimated scattering cell phase centre (for the pixel of interest) at the reference elevation. The dashed concentric arcs show the areas that fall within a given slant-range bin (i.e. the pixel of interest). Because the two receive antennas observe the ground plane from slightly different angles, they do not necessarily simultaneously illuminate the same set of scatterers. Points **D** and **E** are the actual phase centres of the scattering cell as observed from antennas A and B, respectively, which illustrates the phase centre of the scattering cell differing as observed from each antenna. The level to which the phase centres differ is a measure of geometric decorrelation (Duersch and Long 2015).

Given that the two antennas may observe slightly different locations for the phase centre of the scattering cell, this article proceeds with a derivation of the interferometric height resulting from backprojected residual phase. The interferometer geometry is given in Figure 1(*b*). Here, r is the estimated range from the receive antenna to the scattering cell phase centre and r' is the actual range to the scattering cell phase centre. The three-dimensional displacement vector $\boldsymbol{\delta}$ $\left(\delta_x, \delta_y, \delta_z\right)$ is the offset from **C** to **D** and ϵ is the displacement from **D** to **E**. Hence,

$$\mathbf{D} = \mathbf{C} - \boldsymbol{\delta}, \tag{3}$$

$$\mathbf{E} = \mathbf{C} - (\boldsymbol{\delta} + \epsilon). \tag{4}$$

In general, $\boldsymbol{\delta}$ and ϵ are unknown. In this derivation, $\boldsymbol{\delta}$ is the interferometric displacement from which height information is obtained. Although not used here, θ is the incidence angle to the scattering cell and α is the interferometric angular baseline. These variables become important later in this section to parameterize traditional interferometry.

The backprojected residual ranges Δr are defined as

$$\Delta r_a = r_a - r'_a, \tag{5}$$

$$\Delta r_b = r_b - r'_b. \tag{6}$$

These ranges are given by the distances to the various points:

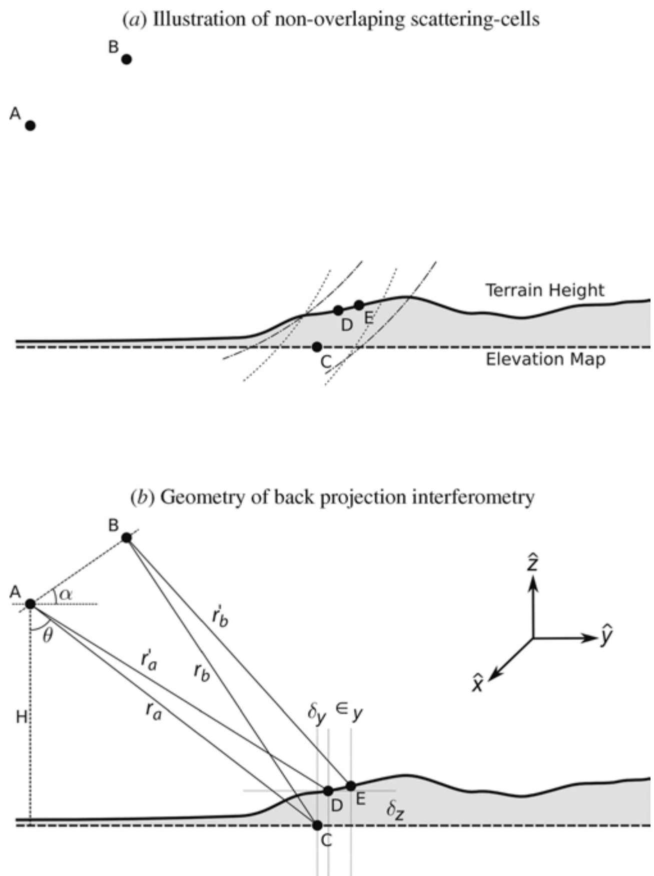

Figure 1. Exaggerated illustration of scattering cell phase centre differences in interferometry. The axes $\hat{x}$, $\hat{y}$, and $\hat{z}$ represent along-track, cross-track, and elevation, respectively. Receive antennas are located at points **A** and **B**. Point **C** is the estimated phase centre of the scattering cell given coarse knowledge of the topography (e.g. a DEM). Points **D** and **E** are the actual phase centres of the scattering cell observed by antennas at **A** and **B**, respectively. Notice that because the two antennas are not collocated, they observe a slightly different set of scatterers within the resolution cell.

$$r_a = \|\mathbf{C} - \mathbf{A}\| = \sqrt{(x_a - x_c)^2 + (y_a - y_c)^2 + (z_a - z_c)^2}, \tag{7}$$

$$r'_a = \|\mathbf{D} - \mathbf{A}\| = \sqrt{(x_a - x_d)^2 + (y_a - y_d)^2 + (z_a - z_d)^2}, \tag{8}$$

$$r_b = \|\mathbf{C} - \mathbf{B}\| = \sqrt{(x_b - x_c)^2 + (y_b - y_c)^2 + (z_b - z_c)^2}, \tag{9}$$

$$r'_b = \|\mathbf{E} - \mathbf{B}\| = \sqrt{(x_b - x_e)^2 + (y_b - y_e)^2 + (z_b - z_e)^2}, \tag{10}$$

with x in along-track, y in ground-range, and z in elevation. The actual range from receive antenna A to the phase centre of the scatter cell is

$$r'_a = \sqrt{(x_a - x_c - \delta_x)^2 + \left(y_a - y_c - \delta_y\right)^2 + (z_a - z_c - \delta_z)^2}$$
$$= \left(\begin{array}{c} (x_a - x_c)^2 + (y_a - y_c)^2 + (z_a - z_c)^2 - \\ \delta_x(2(x_a - x_c) - \delta_x) - \delta_y\left(2(y_a - y_c) - \delta_y\right) - \delta_z(2(z_a - z_c) - \delta_z) \end{array} \right)^{1/2} \tag{11}$$

$$= \sqrt{r_a^2 - \delta_x(2(x_a - x_c) - \delta_x) - \delta_y\left(2(y_a - y_c) - \delta_y\right) - \delta_z(2(z_a - z_c) - \delta_z)}. \tag{12}$$

Using the first-order Taylor series approximation for the square root $\sqrt{m^2 + n} \approx m + n/(2m)$, this becomes

$$r'_a \approx r_a - \frac{\delta_x(2(x_a - x_c) + \delta_x) + \delta_y\left(2(y_a - y_c) + \delta_y\right) + \delta_z(2(z_a - z_c) + \delta_z)}{2r_a}. \tag{13}$$

The first-order Taylor series approximation is highly accurate near the point of closest approach, and it works well for a non-squinted geometry (see Duersch 2013). The squinted geometry case is beyond the scope of this article since there is no closed-form solution for the squinted residual phase.

As the range from the receive antennas to the scattering cell is presumed to be much larger than the phase centre displacement, Equation (13) can be reduced further to

$$r'_a \approx r_a - \frac{\delta_x(x_a - x_c) + \delta_y(y_a - y_c) + \delta_z(z_a - z_c)}{r_a}. \tag{14}$$

Likewise, for antenna B,

$$r'_b \approx r_b - \frac{(\delta_x + \epsilon_x)(x_b - x_c) + \left(\delta_y + \epsilon_y\right)(y_b - y_c) + (\delta_z + \epsilon_z)(z_b - z_c)}{r_b}. \tag{15}$$

Substituting these into the range residuals yields

$$\begin{aligned} \Delta r_a &= r_a - r'_a \\ &= \frac{\delta_x(x_a - x_c) + \delta_y(y_a - y_c) + \delta_z(z_a - z_c)}{r_a}, \end{aligned} \tag{16}$$

$$\begin{aligned} \Delta r_b &= r_b - r'_b \\ &= \frac{(\delta_x + \epsilon_x)(x_b - x_c) + \left(\delta_y + \epsilon_y\right)(y_b - y_c)}{r_b} + \frac{(\delta_z + \epsilon_z)(z_b - z_c)}{r_b}. \end{aligned} \tag{17}$$

Inserting Δr_a and Δr_b into the interferometric phase $\Delta\Phi = k(\Delta r_a - \Delta r_b)$ results in one equation with six unknowns because the three-dimensional phase centre displacements $\boldsymbol{\delta}$ and ϵ are unknown. Under some simplifying assumptions, this may be reduced to one unknown.

A key assumption in interferometry is that the pixels, as imaged from the two antennas, are highly correlated. This requires that the baseline separation not be too great (Duersch and Long 2015). The assumption that the pixel correlation is high requires that the scattering cell phase centre be nearly the same when viewed from both receive antennas. In other words, the ϵ terms are approximately zero. When $\epsilon \approx 0$ (i.e. the phase centre as observed from the second antenna is collocated with that of the first antenna), the interferometric phase reduces to

$$\begin{aligned}\frac{\Delta\Phi}{2k} &= \frac{\delta_x(x_a - x_c) + \delta_y(y_a - y_c) + \delta_z(z_a - z_c)}{r_a} - \frac{\delta_x(x_b - x_c) + \delta_y(y_b - y_c) + \delta_z(z_b - z_c)}{r_b} \\ &= \delta_x\left(\frac{x_a - x_c}{r_a} - \frac{x_b - x_c}{r_b}\right) + \delta_y\left(\frac{y_a - y_c}{r_a} - \frac{y_b - y_c}{r_b}\right) + \delta_z\left(\frac{z_a - z_c}{r_a} - \frac{z_b - z_c}{r_b}\right).\end{aligned} \tag{18}$$

Solving for the height displacement δ_z results in

$$\delta_z = \frac{\frac{\Delta\Phi}{2k} - \delta_x\left(\frac{x_a - x_c}{r_a} - \frac{x_b - x_c}{r_b}\right) - \delta_y\left(\frac{y_a - y_c}{r_a} - \frac{y_b - y_c}{r_b}\right)}{\left(\frac{z_a - z_c}{r_a} - \frac{z_b - z_c}{r_b}\right)} \tag{19}$$

$$\begin{aligned}&= \frac{\Delta\Phi\, r_a r_b}{2k(r_b(z_a - z_c) - r_a(z_b - z_c))} - \delta_x \frac{r_b(x_a - x_c) - r_a(x_b - x_c)}{r_b(z_a - z_c) - r_a(z_b - z_c)} \\ &\quad - \delta_y \frac{r_b(y_a - y_c) - r_a(y_b - y_c)}{r_b(z_a - z_c) - r_a(z_b - z_c)},\end{aligned} \tag{20}$$

which is one equation with three unknowns (δ_x, δ_y, and δ_z).

For now, assume that $\delta_x \approx 0$ and $\delta_y \approx 0$. The consequences of this assumption are discussed in Section 4.2. With this assumption, there is only one unknown, which is the estimated height offset $\widetilde{\delta}_z$ for the scattering cell:

$$\widetilde{\delta}_z = \frac{\Delta\Phi\, r_a r_b}{2k(r_b(z_a - z_c) - r_a(z_b - z_c))}. \tag{21}$$

Note that in this case the height displacement may be computed without the use of trigonometric functions. However, recognizing that with incidence angle θ, $r_a \cos\theta_a = (z_a - z_c)$ and $r_b \cos\theta_b = (z_b - z_c)$, the height estimate may also be written as

$$\widetilde{\delta}_z = \frac{\Delta\Phi\, r_a r_b}{2k(r_b r_a \cos\theta_a - r_a r_b \cos\theta_b)}, \tag{22}$$

$$= \frac{\Delta\Phi}{2k\ (\cos\theta_a - \cos\theta_b)}. \tag{23}$$

The traditional interferometric phase for single-pass, fixed-baseline SAR is (Rosen et al. 2000; Bamler and Just 1993)

$$\Phi = kB\sin(\theta - \alpha), \tag{24}$$

$$\theta = \arccos\left(\frac{H - \delta_z}{r}\right), \tag{25}$$

where Φ is the traditional interferometric phase difference, B is the baseline distance between the receive antennas, α is the angular difference between the antennas with respect to the horizontal plane, and H is the interferometer height above the reference plane. This leads to the height estimate

$$\begin{aligned}\widetilde{\delta}_z &= H - r\cos\theta,\\ &= H - r\cos\left(\alpha + \arcsin\frac{\Phi}{kB}\right).\end{aligned} \tag{26}$$

A cursory comparison of Equations (21) and (26) reveals that the interferometric height estimate from backprojection is linear with phase, while the traditional method is nonlinear. The following section compares both interferometric methods and presents their respective sensitivities.

3. Sensitivity comparison

This section examines the height estimate sensitivity of backprojection and traditional interferometry. First, the parameter sensitivity of both methods is derived. Next, a basis for comparing the two methods is provided by assaying the sensitivity to the geometric and phase input parameters. Finally, this section concludes with an examination of baseline and phase errors, which are of specific concern when using interferometry.

3.1. Sensitivity derivation

The sensitivity of the interferometry method to its geometric parameters is found by taking the partial derivative of the height estimate $\widetilde{\delta}_z$ with respect to each variable of interest. To simplify notation, the ~ on $\widetilde{\delta}_z$ is discarded below. For traditional SAR interferometry, computing the partials of Equation (26) results in

$$\frac{\partial\delta_z}{\partial\Phi} = \frac{r\sin\theta}{kB\sqrt{1 - \left(\frac{\Phi}{kB}\right)^2}} = \frac{r\sin\theta}{kB\cos(\theta - \alpha)}, \tag{27}$$

$$\frac{\partial\delta_z}{\partial B} = -\frac{\Phi r\sin\left(\alpha + \arcsin\frac{\Phi}{kB}\right)}{kB^2\sqrt{1 - \left(\frac{\Phi}{kB}\right)^2}} = -\frac{r}{B}\tan(\theta - \alpha)\sin\theta, \tag{28}$$

$$\frac{\partial\delta_z}{\partial\alpha} = r\sin\left(\alpha + \arcsin\frac{\Phi}{kB}\right) = r\sin\theta, \tag{29}$$

$$\frac{\partial \delta_z}{\partial \theta} = r \sin \theta, \tag{30}$$

$$\frac{\partial \delta_z}{\partial r} = -\cos \theta. \tag{31}$$

Notice that the height sensitivities to baseline angle $\frac{\partial \delta_z}{\partial \alpha}$ and incidence angle $\frac{\partial \delta_z}{\partial \theta}$ are identical.

In order to compare the traditional sensitivity results to those of backprojection, Equation (23) must be rewritten in terms of baseline length and angle. From Figure 1, the paths from the antennas to the cell centre **C** and to each other form a triangle. Using the law of sines,

$$\frac{r_a}{\sin\left(\frac{\pi}{2} - \alpha + \theta_b\right)} = \frac{B}{\sin\,(\theta_a - \theta_b)}, \tag{32}$$

$$\sin(\theta_a - \theta_b) = \frac{B}{r_a} \cos\,(\theta_b - \alpha),$$

$$\theta_a = \theta_b + \arcsin\left(\frac{B}{r_a} \cos\,(\theta_b - \alpha)\right). \tag{33}$$

Let γ be the incidence angle difference between the two antennas, i.e.

$$\gamma = \theta_a - \theta_b \tag{34}$$

$$= \arcsin\left(\frac{B}{r_a} \cos(\theta_b - \alpha)\right), \tag{35}$$

then Equation (23) may be rewritten as

$$\delta_z = \frac{\Delta\Phi}{2k[\cos(\theta_b + \gamma) - \cos \theta_b]}. \tag{36}$$

The backprojection sensitivities are found by taking the partial derivatives of Equation (36) with respect to each parameter:

$$\frac{\partial \delta_z}{\partial \Delta\Phi} = \frac{1}{2k(\cos \theta_a - \cos \theta_b)}, \tag{37}$$

$$\begin{aligned} \frac{\partial \delta_z}{\partial B} &= \frac{\Delta\Phi\ \sin(\theta_b + \gamma)}{2k(\cos(\theta_b + \gamma) - \cos\ \theta_b)^2} \frac{\cos\,(\theta_b - \alpha)}{r_a \sqrt{1 - \sin^2\gamma}} \\ &= \frac{\delta_z k(\cos \theta_a - \cos \theta_b) \sin \theta_a \cos(\theta_b - \alpha)}{k r_a (\cos \theta_a - \cos \theta_b)^2 \cos \gamma} \\ &= \delta_z \frac{\sin \theta_a \cos(\theta_b - \alpha)}{r_a \cos \gamma (\cos \theta_a - \cos \theta_b)}, \end{aligned} \tag{38}$$

Table 1. Interferometric sensitivities.

	Traditional	Backprojection
$\frac{\partial \delta_z}{\partial \Phi}$	$\frac{r \sin \theta}{kB \cos(\theta - \alpha)}$	N/A
$\frac{\partial \delta_z}{\partial \Delta\Phi}$	N/A	$\frac{1}{2k(\cos \theta_a - \cos \theta_b)}$
$\frac{\partial \delta_z}{\partial B}$	$-\frac{r}{B}\tan(\theta - \alpha) \sin \theta$	$\delta_z \frac{\sin \theta_a \cos(\theta_b - \alpha)}{r_a \cos \gamma (\cos \theta_a - \cos \theta_b)}$
$\frac{\partial \delta_z}{\partial \alpha}$	$r \sin \theta$	$\delta_z \frac{B \sin \theta_a \sin(\theta_b - \alpha)}{r_a \cos \gamma (\cos \theta_a - \cos \theta_b)}$
$\frac{\partial \delta_z}{\partial r_a}$	$-\cos \theta$	$-\delta_z \frac{B \sin \theta_a \cos(\theta_b - \alpha)}{r_a^2 \cos \gamma (\cos \theta_a - \cos \theta_b)}$
$\frac{\partial \delta_z}{\partial \theta_b}$	$r \sin \theta$	$-\delta_z \frac{\left(\frac{B \sin(\theta_b - \alpha)}{r_a \cos \gamma} - 1\right) \sin \theta_a + \sin \theta_b}{\cos \theta_a - \cos \theta_b}$

$$\begin{aligned}\frac{\partial \delta_z}{\partial \alpha} &= \frac{\Delta\Phi \ \sin(\theta_b + \gamma)}{2k(\cos(\theta_b + \gamma) - \cos \theta_b)^2} \frac{B \sin(\theta_b - \alpha)}{r_a \sqrt{1 - \sin^2 \gamma}} \\ &= \delta_z \frac{B \sin \theta_a \sin(\theta_b - \alpha)}{r_a \cos \gamma (\cos \theta_a - \cos \theta_b)},\end{aligned} \tag{39}$$

$$\begin{aligned}\frac{\partial \delta_z}{\partial r_a} &= -\frac{\Delta\Phi \ \sin(\theta_b + \gamma)}{2k(\cos(\theta_b + \gamma) - \cos \theta_b)^2} \frac{B \cos(\theta_b - \alpha)}{r_a^2 \sqrt{1 - \sin^2 \gamma}} \\ &= -\delta_z \frac{B \sin \theta_a \cos(\theta_b - \alpha)}{r_a^2 \cos \gamma (\cos \theta_a - \cos \theta_b)},\end{aligned} \tag{40}$$

$$\begin{aligned}\frac{\partial \delta_z}{\partial \theta_b} &= -\frac{\Delta\Phi \left(\sin(\theta_b + \gamma) \left(\frac{B \sin(\theta_b - \alpha)}{r_a \sqrt{1 - \sin^2 \gamma}} - 1 \right) + \sin \theta_b \right)}{2k(\cos(\theta_b + \gamma) - \cos \theta_b)^2} \\ &= -\delta_z \frac{\left(\frac{B \sin(\theta_b - \alpha)}{r_a \cos \gamma} - 1 \right) \sin \theta_a + \sin \theta_b}{\cos \theta_a - \cos \theta_b}.\end{aligned} \tag{41}$$

We observe that the sensitivity equations for backprojection are more complicated than the traditional approach. The sensitivities of both methods are given side-by-side in Table 1.

3.2. Sensitivity analysis

The backprojection sensitivity equations are more complicated than those of the traditional method, which makes a direct comparison of the sensitivities difficult. However, two observations may be made in general: (1) in all but phase, backprojection sensitivity is directly proportional to vertical displacement of the target. This implies that if the target displacement is small (i.e. the initial DEM is accurate), then backprojection sensitivity to the geometry parameters is likewise small. This is a critical insight as traditional interferometry is extremely sensitive to errors in baseline length and angle. (2) Where range appears in the sensitivity equations, it always appears in the numerator in traditional interferometry while in backprojection it always appears in the denominator. Therefore, as range increases, the sensitivity of backprojection interferometry to the other parameters decreases.

For these two reasons, backprojection is less sensitive than traditional interferometry to the geometric errors: baseline length, baseline angle, range to target, and incidence angle. However, as shown later, for most imaging scenarios backprojection is more sensitive to phase errors than traditional interferometry, and indeed phase error is the primary limiting factor in the accuracy of backprojection height estimation.

A detailed comparison of sensitivities is somewhat tedious (Duersch 2013). For brevity, only the highlights and key observations from Duersch (2013) are given here. Figure 2, comparing the sensitivity of both interferometric methods, illustrates many of the points given below. The geometry parameters used are an incidence angle $\theta = 53°$, antenna baseline length $B = 2$ m, baseline angle $\alpha = 30°$ and $\alpha = 60°$, range-to-target $r_a = 10$ km, and vertical displacement $\delta_z = 500\lambda$. Phase sensitivity is evaluated at Ku-band ($\lambda = 1.9$ cm).

- In the interferometric methods, for a given sensitivity parameter, certain incidence angles perform particularly well. These incidence angles are termed *sweet spots*. For both interferometric methods, a sweet spot occurs when the interferometric baseline angle equals the incidence angle. In addition, for traditional interferometry a sweet spot occurs in baseline length sensitivity (i.e. $\tan(\theta - \alpha) = 0$ in Equation (28)), while for backprojection interferometry it occurs in baseline angle sensitivity (i.e. $\sin(\theta_b - \alpha) = 0$ in Equation (39)).
- Unlike traditional interferometry, backprojection has a second sweet spot in sensitivity to incidence angle. This sweet spot occurs at incidence angle

$$\theta_a = \arcsin\left[-\left(\frac{B\sin(\theta_b - \alpha)}{r_a\cos(\theta_a - \theta_b)} - 1\right)^{-1}\sin(\theta_b)\right], \tag{42}$$

which comes from the numerator of Equation (41).

- The sensitivity of backprojection to the physical parameters (baseline length, baseline angle, range-to-target) is orders of magnitude lower than traditional. However, for typical SAR incidence angles, backprojection is about twice as sensitive to interferometric phase as traditional interferometry.
- The height estimate accuracy of traditional interferometry is better at shallow incidence angles (near 0°) as opposed to backprojection interferometry, which is better at large incidence angles (near 90°).
- Backprojection interferometry obtains the biggest improvement in height estimate accuracy for long range and when the height offset is small. If the DEM is accurate, then backprojection provides a better estimate of the height offset than the traditional method.

Errors in phase or baseline measurement significantly affect interferometry performance, so they are discussed in more depth in the following subsections.

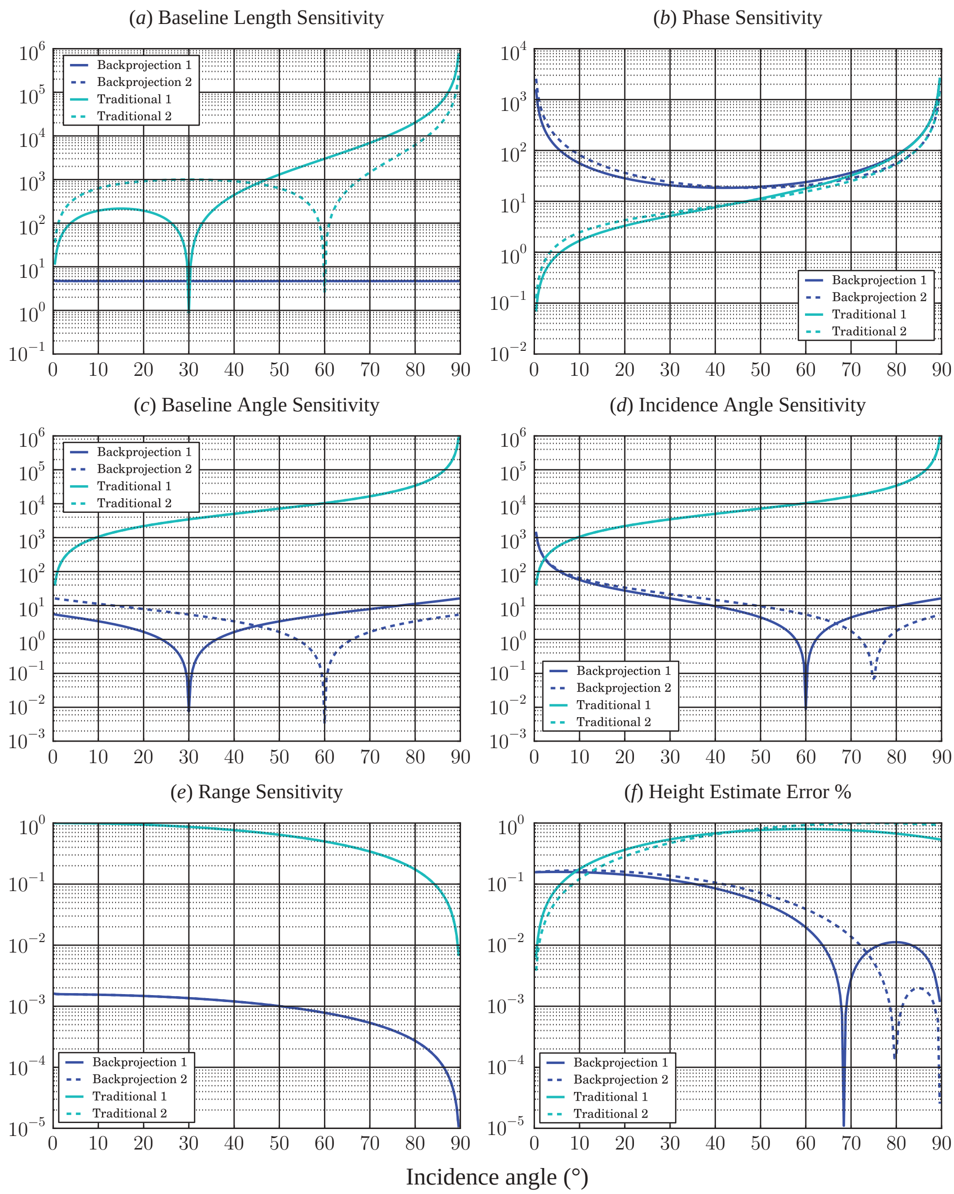

Figure 2. Sensitivity comparison of traditional and backprojection interferometry for two baseline angles. The solid lines correspond to a 30° baseline and the dashed lines correspond to 60° baseline. Where there is no change, the dashed lines are not visible.

3.3. Baseline error comparison

While the brief sensitivity observations of the previous section provide some insight into the performance of both interferometric approaches, the following two subsections more closely investigate the height estimate accuracy of both methods. This subsection specifically examines the effects of errors in measurement of the baseline length and baseline angle. The analysis confirms that traditional interferometry is extremely sensitive to errors in these baseline parameters, while backprojection interferometry is much less sensitive.

Below, we examine the height estimate error for several types/magnitudes of baseline error. Rather than examine one particular incidence angle, the minimum and maximum error for each interferometric method is calculated across 30° to 60°. In the figures, the minimum curves represent the performance at the sweet spot of the method, while the maximum curves represent the performance away from the sweet spot.

Figure 3 gives the height estimation error for both interferometric methods as a function of range-to-target. The parameters are λ = 3 cm, baseline angle $\alpha = 45°$, and a target displacement of 10 m from the DEM. Figures 3(a) and (b) illustrate the effects of error in the measurement of the interferometric baseline angle for a baseline length of 1 m. The baseline angle error in (a) is 0.0001 rad and in (b) is 0.001 rad. Errors of this magnitude are commensurate with those of a low-altitude platform where a combination of non-ideal motion and errors in attitude measurement lead to errors in the measurement of the baseline angle. For a small range-to-target, the traditional method has lower error than the backprojection method; however, the error increases as the range-to-target increases, and between 200 and 700 m backprojection begins to outperform it. If the baseline length is increased, then backprojection surpasses the traditional method in

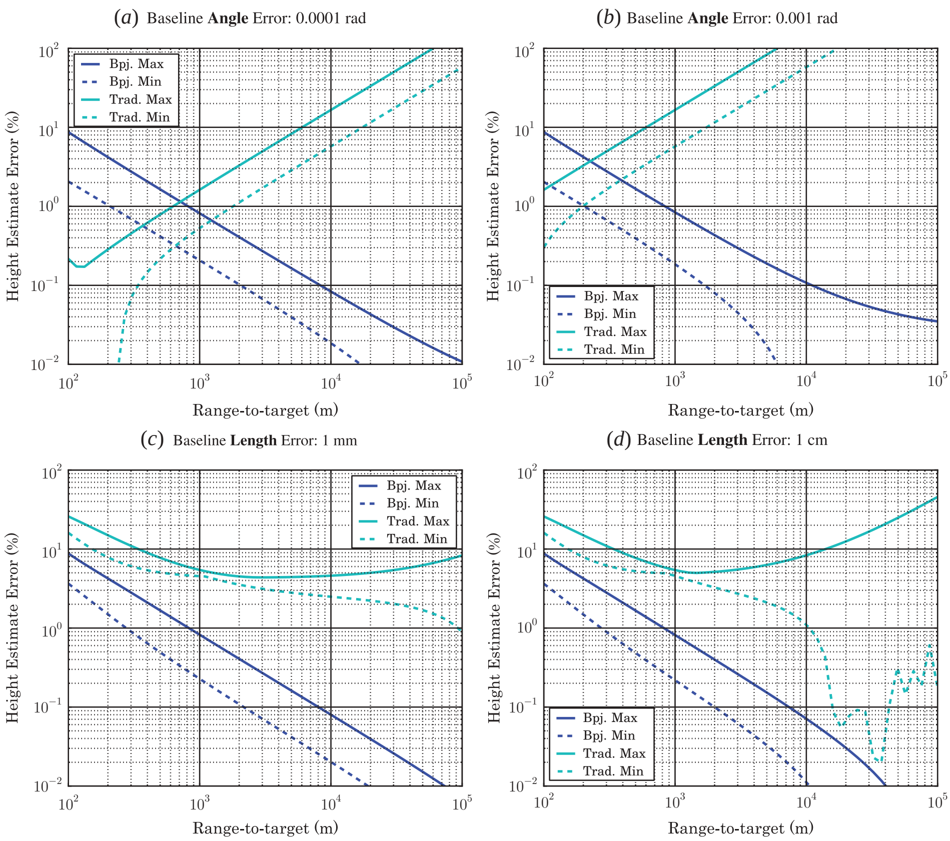

Figure 3. Comparison of the effects of baseline errors on the interferometric height estimate as a function of range-to-target. (a) and (b) The effect of angular baseline error with a baseline of length 1 m. (c) and (d) The effect of baseline length error with a baseline length of 100 m. The nominal baseline angle is 45°. The maximum and minimum are taken across the range of incidence angles 30° to 60°.

Note: Bpj., backprojection; Trad., traditional.

performance, even at smaller ranges. It is important to note that if there is significant uncertainty in measurement of the baseline angle, then the sweet spot of the traditional approach might go unutilized and the performance would be closer to the maximum error than the minimum error.

Figures 3(*c*) and (*d*) show the effects of error in measurement of the interferometric baseline length for a nominal baseline length of 100 m. This geometry is more suggestive of a high-altitude interferometer. In (*c*), the error in measurement of the baseline length is 1 mm and in (*d*) is 1 cm. Because of the large baseline, even at near ranges the maximum backprojection error is less than the traditional method's error. The maximum error in the traditional method decreases until an inflection point where it begins to grow large again. For a large range-to-target, the minimum goes to zero (i.e. no error) at the sweet spot of $\alpha = \theta$. In the high-altitude case, it may be realistic for most of the range swath to fall within this sweet-spot.

Notice that in all the cases the error in backprojection height estimate decreases as the range-to-target increases. Notice also that in each case the performance of backprojection shows little variation while the performance of the traditional method varies widely. This reinforces the conclusion of the previous subsection that backprojection is less sensitive to errors in measurement of the interferometric baseline, while the opposite is true for the traditional method.

3.4. Phase noise comparison

This subsection compares how errors in the interferometric phase measurement affect both methods. The variance of the phase error is approximately the same for both methods despite the fact that traditional interferometry utilizes Φ, while backprojection interferometry utilizes $\Delta\Phi$. In the case of $\Delta\Phi$, subtracting the assumed phase (computed using the DEM) during image formation does not affect the variance of the phase noise.

Figure 4 compares the effects of interferometric phase error on both methods. In each, the wavelength $\lambda = 3$ cm, the baseline angle $\alpha = 45°$, and the height from the DEM $\delta_z = 10$ m. As before, the minimum and maximum of each method is taken from 30 to 60°. Figures 4(*a*)–(*c*) have 10° of phase error, while (*d*) has 1°. The baseline lengths in (*a*)–(*d*) are 1, 10, 100, and 10 m, respectively.

In (*a*), (*b*), and (*d*) (i.e. 10 m baseline and shorter), the maximum backprojection height estimate error is worse than the traditional method. At a 100 m baseline in (*c*), the performance of backprojection exceeds the traditional method for smaller ranges to target (where the approximations in traditional interferometry are invalid), but at larger ranges the traditional method again outperforms backprojection. Whereas with baseline errors where backprojection's estimate improves with increasing range, the backprojection estimate degrades with range for large ranges. Even in (*d*), where the phase error is quite small, the traditional method attains a better estimate than backprojection. It is evident that while both interferometry methods are sensitive to phase errors, backprojection is more sensitive than the traditional.

4. Interferometry performance

The following subsections describe specific performance aspects of time-domain backprojection interferometry. The first subsection introduces the concept of the *transition baseline*, which is the minimum interferometric baseline length for which the performance of backprojection interferometry surpasses conventional interferometry. The next

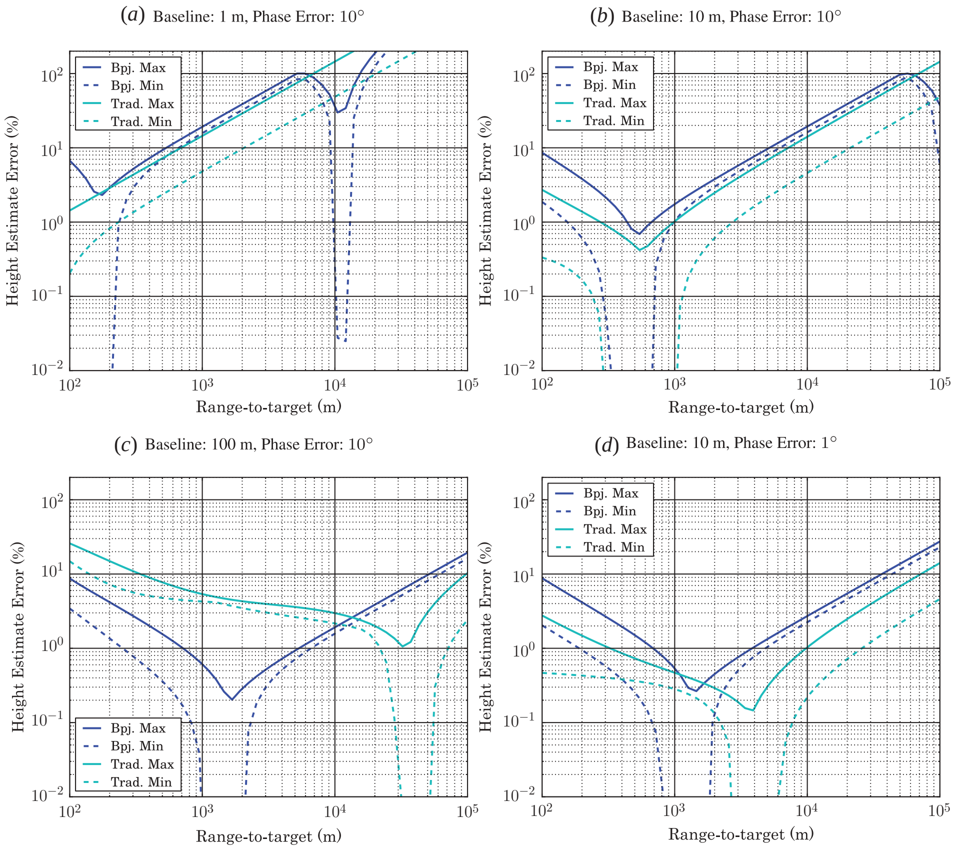

Figure 4. Comparison of the effects of phase error for both interferometric methods as a function of range-to-target. The minimum and maximum error percentage are computed from incidence angles 30° to 60°. The model parameters are $\lambda = 3$ cm, $\alpha = 45°$, and $\delta_z = 10$ m. (a)–(c) have 10° of phase error, while (d) has 1°. The baseline lengths in (a)–(d) are 1, 10, 100, and 10 m, respectively.

subsection describes the effects of phase centre shift in each of the dimensions, azimuth, range, and elevation. The final subsection considers the effects of DEM accuracy.

4.1. Transition baseline

Backprojection interferometry outperforms traditional interferometry for a long baseline. It is possible to approximate the minimum baseline length where the height estimation accuracy of backprojection exceeds that of traditional interferometry. While both methods suffer from height estimation errors due to phase measurement errors, the height estimate of conventional interferometry also has errors due to baseline length and baseline angle measurement errors.

To estimate the transition baseline, the baseline length B is determined such that the major contributing errors of both interferometric methods are equal. Thus, setting $\partial\delta_z$ from Equation (37) (the backprojection phase sensitivity) equal to the sum of $\partial\delta_z$ from Equations (27) through (29) (the phase and geometric sensitivities of the traditional method), the transition baseline length B may be found through use of a numerical root solver if

$$\frac{\partial\Delta\Phi}{k(\cos\theta_a-\cos\theta_b)}=\partial\Phi\frac{r\sin\theta}{kB\cos(\theta-\alpha)}-\partial B\frac{r}{B}\tan(\theta-\alpha)\sin\theta+\partial\alpha(r\sin\theta)$$

$$=r\sin\theta_a\left[\frac{\partial\Phi}{kB\cos(\theta_a-\alpha)}-\frac{\partial B}{B}\tan(\theta_a-\alpha)+\partial\alpha\right], \tag{43}$$

$$0=\frac{k(\cos\theta_a-\cos\theta_b)}{\partial\Delta\Phi}r\sin\theta_a\cdot$$

$$\left(\frac{\partial\Phi}{kB\cos(\theta_a-\alpha)}-\frac{\partial B}{B}\tan(\theta_a-\alpha)+\partial\alpha\right)-1. \tag{44}$$

This expression may be simplified if the interferometric angular baseline $\alpha\approx 45°$. Assuming this to be the case,

$$\theta_b\approx\arccos\left(\cos\theta_a+\frac{B\cos\alpha}{r_a}\right). \tag{45}$$

Additionally, let

$$\Gamma\,\partial\Phi=\partial\Delta\Phi, \tag{46}$$

where the constant Γ represents the ratio of phase difference error to phase error. Substituting these into Equation (44),

$$\begin{aligned}\Gamma=&\ \frac{k}{\partial\Phi}\left(\frac{-B\cos\alpha}{r_a}\right)\ r_a\sin\theta_a\left(\frac{\partial\Phi}{kB\cos(\theta_a-\alpha)}-\frac{\partial B}{B}\tan(\theta_a-\alpha)+\partial\alpha\right)\\ =&\ -kB\cos\alpha\sin\theta_a\left(\frac{1}{kB\cos(\theta_a-\alpha)}-\frac{\partial B}{\partial\Phi}\frac{1}{B}\tan(\theta_a-\alpha)+\frac{\partial\alpha}{\partial\Phi}\right)\\ =&\ -\frac{\cos\alpha\sin\theta_a}{\cos(\theta_a-\alpha)}+\frac{\partial B}{\partial\Phi}k\cos\alpha\sin\theta_a\tan(\theta_a-\alpha)-\frac{\partial\alpha}{\partial\Phi}kB\cos\alpha\sin\theta_a.\end{aligned}$$

Rearranging and solving for B,

$$\begin{aligned}\frac{\partial\alpha}{\partial\Phi}kB\cos\alpha\sin\theta_a=&\ \frac{\partial B}{\partial\Phi}k\cos\alpha\sin\theta_a\tan(\theta_a-\alpha)-\frac{\cos\alpha\sin\theta_a}{\cos(\theta_a-\alpha)}-\Gamma,\\ B=&\ \frac{\partial\Phi}{\partial\alpha}\frac{1}{k\cos\alpha\sin\theta_a}\left[\frac{\partial B}{\partial\Phi}k\cos\alpha\sin\theta_a\tan(\theta_a-\alpha)-\frac{\cos\alpha\sin\theta_a}{\cos(\theta_a-\alpha)}-\Gamma\right]\\ =&\ \frac{\partial B}{\partial\alpha}\tan(\theta_a-\alpha)-\frac{\partial\Phi}{\partial\alpha}\left(\frac{1}{k\cos(\theta_a-\alpha)}+\frac{\Gamma}{k\cos\alpha\sin\theta_a}\right).\end{aligned} \tag{47}$$

Recall that this expression is only valid near $\alpha=45°$. For angular baselines away from this angle, Equation (44) must be solved directly. In these equations, the sensitivity to range measurement error has been neglected as it is assumed to be insignificant. If it becomes a significant error source, then the transition baseline is shorter than that given

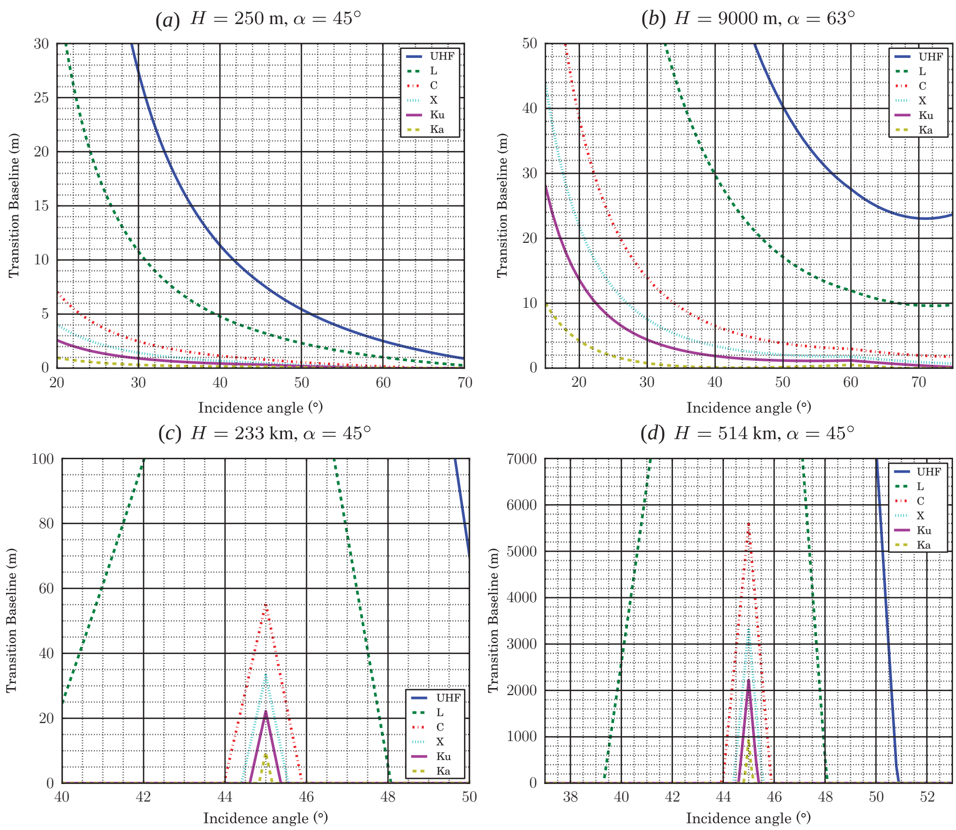

Figure 5. Comparison of baseline transition region for several geometries across various frequency bands.

above. Note that while the ratios $\partial B/\partial\Phi$ and $\partial\alpha/\partial\Phi$ are written as partial derivatives, they are better thought of as ratios of errors (i.e. the ratio of baseline-length error to baseline-angle error and phase error to baseline-angle error, respectively). Also note that while calculation of the transition baseline indicates the length for which backprojection performs better, in practice, both interferometric methods perform approximately the same for lengths near the transition baseline.

Figure 5 shows the transition baseline length for several prevalent geometries at various frequency bands through computing Equation (44).

The carrier frequency for the bands used are UHF: 650 MHz, L: 1.5 GHz, C: 6 GHz, X: 10 GHz, K_u: 15 GHz, and K_a: 35 GHz. The geometries in Figures 5(*a*)–(*d*) represent cases (1), (3), (4), and (5) in Table 2, respectively. The errors used in each model are also given in the table. Note that the values for these errors do not necessarily represent the error for a particular system, but rather indicate possible values for purposes of comparison. For a given frequency, a baseline length above the corresponding curve indicates favourability of backprojection interferometry and those below favour traditional interferometry.

From these examples, several observations may be made. (1) Notice the sweet spot at 45° for traditional interferometry in Figures 5(*c*) and (*d*). The peak here suggests that a longer baseline is required before backprojection becomes advantageous. (2) As the carrier frequency increases, the transition baseline becomes smaller. This implies that

Table 2. Example geometries.

#	Example	Cite	Height	Baseline length (m)	Baseline angle (°)	Light grey $\partial\Phi$	∂B	$\partial\alpha$
1	Small UAV	–	250 m	0.16	45	0.21	0.001	2×10^{-3}
2	Medium UAV	–	500 m	2	90	0.21	0.001	2×10^{-3}
3	TOPSAR	Zebker et al. 1992	8500 m	2.6	62	0.21	0.001	3×10^{-4}
4	SRTM	Farr et al. 2007	233 km	60	45	0.21	0.100	3×10^{-5}
5	TanDEM-X	Krieger et al. 2007	514 km	400	45	0.21	0.100	3×10^{-7}

backprojection interferometry is better suited to high-frequency usage while traditional interferometry is better suited to low-frequency. (3) Overall, the geometries corresponding to Figures 5(*a*) and (*c*) are better suited to backprojection interferometry than (*b*) and (*d*). This is because the geometric uncertainties are large enough to push the transition baseline short enough for the required baseline to be practical.

4.2. Phase centre displacement

In Section 2, in order to eliminate the unknown phase centre displacements in the derivation of backprojection interferometry, it was assumed that the phase centre displacement is solely in the vertical dimension (i.e. $\delta_x = \delta_y = 0$). This subsection explores the consequences of that assumption by evaluating the effect of both vertical and horizontal phase centre displacement on the interferometric height estimate.

Figure 6 demonstrates the computed height estimate for phase centre displacement solely in a given dimension, represented by the three curves. The receive antennas are placed in a horizontal baseline (i.e. $\alpha = 0$), separated by 100 wavelengths, and the incidence angle to the scattering cell is 45°. The vertical axis on the left gives the height

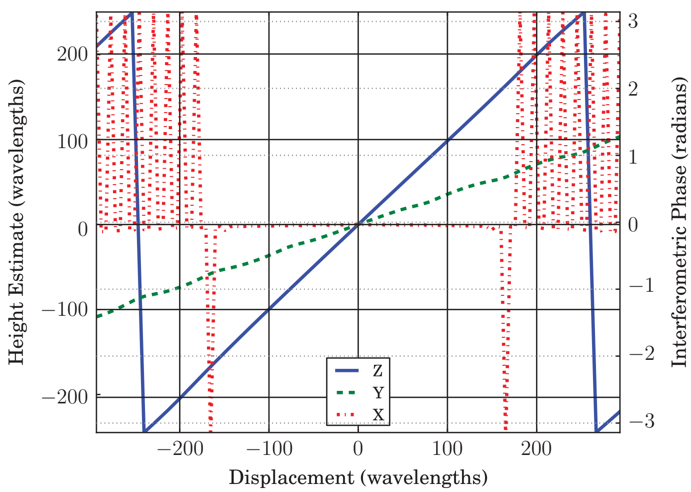

Figure 6. Height estimate resulting from displacement solely in a given dimension for a horizontal baseline of 100 wavelengths.

estimate in wavelengths, and the vertical axis on the right gives the equivalent interferometric phase.

As expected, when the phase centre displacement is strictly in the vertical dimension, the estimated height is equivalent to the vertical displacement. If the phase centre displacement is solely in the ground-range dimension, the estimated height is still linear with displacement, but at a reduced slope compared to that of the vertical displacement. When the displacement is in the along-track dimension, displacement has negligible effect on the height estimate, even at distances greater than the length of the baseline itself. This implies that while phase centre displacement in azimuth may be ignored, displacement in ground-range causes errors in the height estimate of the cell. However, as previously mentioned, for distributed targets the phase centre is likely near the physical centre of the cell so the effect of ground-range displacement is typically be small. On the other hand, as point targets may be physically located anywhere within the scattering cell, they are subject to the greatest uncertainty in height estimation.

4.3. DEM accuracy

This section characterizes the performance of backprojection interferometry with respect to DEM accuracy for various geometries. In doing so, this analysis assumes that the DEM inaccuracy does not significantly affect pixel focus. If the focus is significantly affected, then there may be a drop in signal-to-noise ratio (SNR) or signal-to-clutter ratio (SCR). This may adversely affect the pixel phase and lead to poor interferometry results.

Figure 7 shows plots of normalized interferometric phase $\Delta\Phi/k$ from Equation (21) for various geometries with vertical height displacement from 0.1 to 100 m across all incidence angles. Since the phase is normalized by the carrier wavenumber, horizontal dashed lines are placed in the plot to mark the point where the first phase wrap occurs ($\pm\pi$) for a given frequency. The frequencies corresponding to the named bands are as before: UHF: 650 MHz, *L*: 1.5 GHz, *C*: 6 GHz, *X*: 10 GHz, K_u: 15 GHz, and K_a: 35 GHz. Figures 7(*a*)–(*e*) coincide respectively with rows (1)–(5) in Table 2. Figure 7(*f*) compares the normalized phase Φ/k of traditional interferometry.

Examining the plots, the same general curved shape is seen in each where the normalized phase peaks near 45° incidence and tapers off towards 0° and 90°. A given magnitude of increase in vertical offset increases the phase by the same magnitude. Interestingly, in these examples, even for highly displaced targets (100 m), a single-phase wrap does not occur except at higher frequency bands. This highlights one of the primary advantages of backprojection interferometry: for many geometries, the need for phase unwrapping is either eliminated or trivialized. This may be compared to traditional interferometry in Figure 7(*f*), where all the offset curves appear to overlap (they are in fact separate, but indistinguishable on this scale). Notice the large magnitude of normalized phase. Even a small change in incidence angle across the range swath causes a significant change in phase and leads to rapid phase-wrapping. Indeed, phase unwrapping is a primary concern of traditional interferometry (Rosen et al. 2000).

As discussed in the previous section, phase noise places a fundamental limit on the accuracy of height estimates. For high coherence areas with independent looks (around $n = 4$), it is very reasonable to achieve a phase standard deviation of 10° (Bamler and Hartl 1998). To get an idea of what that means for height estimate accuracy, from the plots in Figure 7, first choose a frequency band. Since the Φ/k wrap lines for that band represent 180°, divide by 10° (the phase standard deviation). That means the minimum distinguishable height lies 18 times (or $10^{1.25}$) lower than the wrap line for the given band.

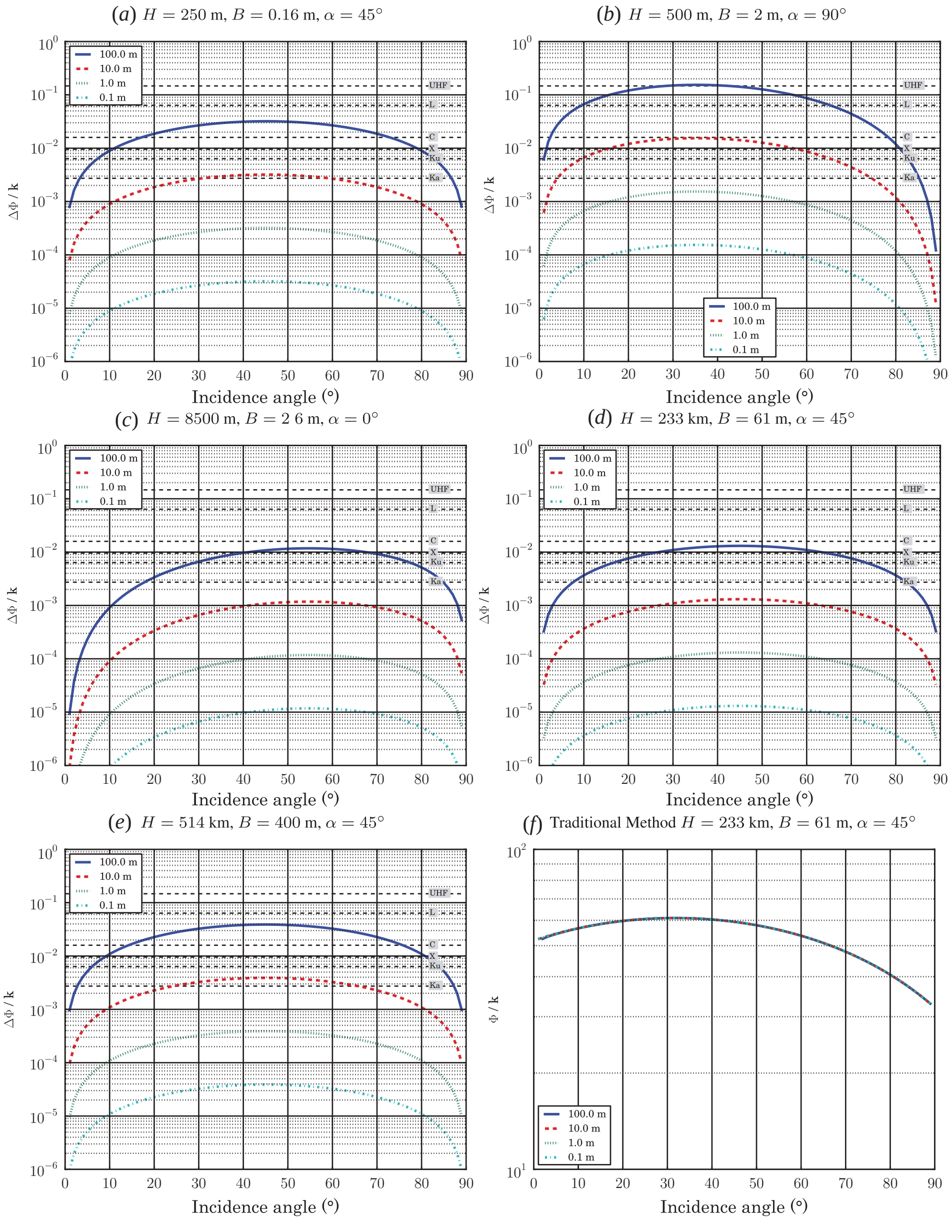

Figure 7. Comparison of normalized interferometric phase Φ/k for various imaging geometries. (a)–(e) represent backprojection interferometry and (f) represents traditional. The subfigure geometries are (a) and (b) low-altitude cases for baselines compatible with small UAVs; (c) similar to TOPSAR; (d) similar to SRTM; (e) similar to TanDEM-X; (f) similar to SRTM using traditional interferometric methods. In (f), the curves are so close they appear to overlap. The horizontal dashed lines represent the normalized phase where the first phase wrap occurs for a given frequency band.

For example, given the geometry in (b), at K_u-band, the minimum discernible height is in the tens of centimetres. The results of these plots confirm the analyses of previous sections: phase noise limits the height estimate accuracy of backprojection interferometry.

5. Discussion

Ideally, the use of backprojection implies that an initial DEM is available. As DEMs are available over most of the surface of the Earth, this is a reasonable assumption. Creation of an initial DEM could be performed via traditional interferometry. The purpose in performing backprojection interferometry is to either refine the DEM or to measure changes in height that have occurred since the DEM was generated. Assuming that a sufficiently accurate DEM is available to generate a focused backprojected image, there are four key advantages to backprojection interferometry.

(1) Backprojection reduces the need for phase unwrapping. As shown at the end of the previous section, the backprojection interferometric phase varies slowly as the cells are displaced from the DEM. Not only does this help eliminate height estimate inaccuracies due to errors in phase unwrapping, but may also lead to the ability to resolve heights of very steep terrain (e.g. urban environments). This is also notably advantageous in low-altitude interferometry where the rapid change in incidence angle across the range swath leads to especially rapid phase-wrapping. Additionally, this is advantageous at higher frequency bands where phase wrapping likewise occurs more rapidly.
(2) As seen in Section 3, backprojection has low sensitivity to errors in the measurement of the interferometry baseline length and angle. This is particularly advantageous at lower altitude applications on an aircraft where turbulence and non-ideal motion lead to errors in the measurement of baseline angle. Where attitude measurement error is pronounced, traditional interferometry can be inaccurate.
(3) Section 3 shows that for conventional interferometry, height estimate errors grow as the baseline length grows. Backprojection interferometry, however, grows in accuracy as the baseline length increases. While an increase in baseline length increases the frequency of phase wraps in the interferogram, the frequency of wrapping is much lower than traditional interferometry and when phase wrapping occurs it may be removed using relatively simple methods.
(4) Backprojection explicitly forms images in the ground plane, making orthorectification unnecessary. As topography can be explicitly included, image artefacts due to terrain relief are reduced, which may also lead to improved accuracy in image analysis and identifying the height of a given location. For example, artefacts like layover may be reduced through backprojection interferometry.

While backprojection interferometry may be advantageous in spaceborne applications, it is especially advantageous at lower altitudes where phase wrapping and errors in baseline measurement are important issues. These problems have commonly made interferometry difficult at lower altitudes, but the use of backprojection may provide an avenue for accurate interferometry at lower altitudes.

6. Conclusion

This article presents a novel method for SAR interferometry using backprojected images. A new interferometric method is required in order to accommodate backprojected images because the backprojected pixel phase corresponds to the difference between the terrain height and the DEM. It is shown that the sensitivity and performance of backprojection interferometry is significantly different than the conventional methods. Specifically, it is shown that backprojection interferometry is much less sensitive to errors in measurement of the interferometric baseline length and angle. This analysis, which shows that backprojection interferometry is particularly well-suited for low-altitude airborne SAR, provides a tool to augment traditional interferometry theory.

Disclosure statement

No potential conflict of interest was reported by the authors.

References

Bamler, R., and D. Just. 1993. "Phase Statistics and Decorrelation in SAR Interferograms." In *International Proceedings of Geoscience and Remote Sensing Symp. IGARSS' 93. Better Understanding of Earth Environment*, Tokyo, August 18–21, 980–984. IEEE. doi:10.1109/IGARSS.1993.322637

Bamler, R., and P. Hartl. 1998. "Synthetic Aperture Radar Interferometry." *Inverse Problems* 14: R1–R54. doi:10.1088/0266-5611/14/4/001.

Duersch, M. I. 2013. "Backprojection for Synthetic Aperture Radar." PhD thesis, Brigham Young University.

Duersch, M. I., and D. G. Long. 2015. "Analysis of Multi-static Pixel Correlation in SAR." *IEEE Transactions on Geoscience and Remote Sensing* 53: 362–374. doi:10.1109/TGRS.2014.2322611.

Farr, T. G., P. A. Rosen, E. Caro, R. Crippen, R. Duren, S. Hensley, M. Kobrick, M. Paller, E. Rodriguez, L. Roth, D. Seal, S. Shaffer, J. Shimada, J. Umland, M. Werner, M. Oskin, D. Burbank, and D. Alsdorf. 2007. "The Shuttle Radar Topography Mission." *Reviews of Geophysics* 45. doi:10.1029/2005RG000183.

Franceschetti, G., and R. Lanari. 1999. *Synthetic Aperture Radar Processing*. Boca Raton, FL: CRC Press.

Krieger, G., A. Moreira, H. Fiedler, I. Hajnsek, M. Werner, M. Younis, and M. Zink. 2007. "TanDEM-X: A Satellite Formation for High-Resolution SAR Interferometry." *IEEE Transactions on Geoscience and Remote Sensing* 45: 3317–3341. doi:10.1109/TGRS.2007.900693.

Li, F. K., and R. M. Goldstein. 1990. "Studies of Multibaseline Spaceborne Interferometric Synthetic Aperture Radars." *IEEE Transactions on Geoscience and Remote Sensing* 28: 88–97. doi:10.1109/36.45749.

Melvin, W. L., and J. A. Scheer. 2013. *Principles of Modern Radar: Advanced Techniques*. Raleigh, NC: SciTech Publishing.

Rodriguez, E., and J. M. Martin. 1992. "Theory and Design of Interferometric Synthetic Aperture Radars." *IEE Proceedings F Radar and Signal Processing* 139: 147–159. doi:10.1049/ip-f-2.1992.0018.

Rosen, P. A., S. Hensley, I. R. Joughin, F. K. Li, S. N. Madsen, E. Rodriguez, and R. M. Goldstein. 2000. "Synthetic Aperture Radar Interferometry." *Proceeding of the IEEE* 88: 333–382. doi:10.1109/5.838084.

Zebker, H., S. Madsen, J. Martin, K. Wheeler, T. Miller, Y. Lou, G. Alberti, S. Vetrella, and A. Cucci. 1992. "The TOPSAR Interferometric Radar Topographic Mapping Instrument." *IEEE Transactions on Geoscience and Remote Sensing* 30: 933–940. doi:10.1109/36.175328.

Zebker, H. A., and R. M. Goldstein. 1986. "Topographic Mapping from Interferometric Synthetic Aperture Radar Observations." *Journal of Geophysical Research: Solid Earth* 91: 4993–4999. doi:10.1029/JB091iB05p04993.

Zebker, H. A., and J. Villasenor. 1992. "Decorrelation in Interferometric Radar Echoes." *IEEE Transactions on Geoscience and Remote Sensing* 30: 950–959. doi:10.1109/36.175330.